



U.S. DEPARTMENT OF  
**ENERGY**

PNNL-23881

Prepared for the U.S. Department of Energy  
under Contract DE-AC05-76RL01830

# Nanocrystalline SiC and $Ti_3SiC_2$ Alloys for Reactor Materials: Diffusion of Fission Product Surrogates

CH Henager, Jr. and W Jiang

November 2014



**Pacific Northwest**  
NATIONAL LABORATORY

*Proudly Operated by **Battelle** Since 1965*

## DISCLAIMER

This report was prepared as an account of work sponsored by an agency of the United States Government. Neither the United States Government nor any agency thereof, nor Battelle Memorial Institute, nor any of their employees, makes **any warranty, express or implied, or assumes any legal liability or responsibility for the accuracy, completeness, or usefulness of any information, apparatus, product, or process disclosed, or represents that its use would not infringe privately owned rights.** Reference herein to any specific commercial product, process, or service by trade name, trademark, manufacturer, or otherwise does not necessarily constitute or imply its endorsement, recommendation, or favoring by the United States Government or any agency thereof, or Battelle Memorial Institute. The views and opinions of authors expressed herein do not necessarily state or reflect those of the United States Government or any agency thereof.

PACIFIC NORTHWEST NATIONAL LABORATORY  
*operated by*  
BATTELLE  
*for the*  
UNITED STATES DEPARTMENT OF ENERGY  
*under Contract DE-AC05-76RL01830*

Printed in the United States of America

Available to DOE and DOE contractors from the  
Office of Scientific and Technical Information,  
P.O. Box 62, Oak Ridge, TN 37831-0062;  
ph: (865) 576-8401  
fax: (865) 576-5728  
email: [reports@adonis.osti.gov](mailto:reports@adonis.osti.gov)

Available to the public from the National Technical Information Service  
5301 Shawnee Rd., Alexandria, VA 22312  
ph: (800) 553-NTIS (6847)  
email: [orders@ntis.gov](mailto:orders@ntis.gov) <<http://www.ntis.gov/about/form.aspx>>  
Online ordering: <http://www.ntis.gov>



This document was printed on recycled paper.

(8/2010)

# **Nanocrystalline SiC and Ti<sub>3</sub>SiC<sub>2</sub> Alloys for Reactor Materials: Diffusion of Fission Product Surrogates**

CH Henager, Jr. and W Jiang

November 2014

Prepared for  
the U.S. Department of Energy  
under Contract DE-AC05-76RL01830

Pacific Northwest National Laboratory  
Richland, Washington 99352

## Abstract

MAX phases, such as titanium silicon carbide ( $\text{Ti}_3\text{SiC}_2$ ), have a unique combination of both metallic and ceramic properties, which make them attractive for potential nuclear applications.  $\text{Ti}_3\text{SiC}_2$  has been suggested in the literature as a possible fuel cladding material. Prior to the application, it is necessary to investigate diffusivities of fission products in the ternary compound at elevated temperatures. This study attempts to obtain relevant data and make an initial assessment for  $\text{Ti}_3\text{SiC}_2$ . Ion implantation was used to introduce fission product surrogates (Ag and Cs) and a noble metal (Au) in  $\text{Ti}_3\text{SiC}_2$ , SiC, and a dual-phase nanocomposite of  $\text{Ti}_3\text{SiC}_2/\text{SiC}$  synthesized at PNNL. Thermal annealing and in-situ Rutherford backscattering spectrometry (RBS) were employed to study the diffusivity of the various implanted species in the materials. In-situ RBS study of  $\text{Ti}_3\text{SiC}_2$  implanted with Au ions at various temperatures was also performed. The experimental results indicate that the implanted Ag in SiC is immobile up to the highest temperature (1273 K) applied in this study; in contrast, significant out-diffusion of both Ag and Au in MAX phase  $\text{Ti}_3\text{SiC}_2$  occurs during ion implantation at 873 K. Cs in  $\text{Ti}_3\text{SiC}_2$  is found to diffuse during post-irradiation annealing at 973 K, and noticeable Cs release from the sample is observed. This study may suggest caution in using  $\text{Ti}_3\text{SiC}_2$  as a fuel cladding material for advanced nuclear reactors operating at very high temperatures. Further studies of the related materials are recommended.

## Summary

This report documents the experimental results from a diffusion study of fission product surrogates (Ag and Cs) and a noble metal (Au) in MAX phase  $\text{Ti}_3\text{SiC}_2$ , cubic/hexagonal SiC, and a dual-phase nanocomposite of  $\text{Ti}_3\text{SiC}_2/\text{SiC}$ . All of the implanted species were observed to be mobile in MAX phase  $\text{Ti}_3\text{SiC}_2$  and to diffuse to the surface at moderately high temperatures (873 -973 K). However, Ag in SiC was observed to be immobile at the highest temperature (1273 K) applied in this study. The results from this study may provide an implication for caution of using  $\text{Ti}_3\text{SiC}_2$  as a fuel cladding material for advanced nuclear reactors operating at very high temperatures.

Implantation of 400 keV  $\text{Ag}^{2+}$ , 2 MeV  $\text{Au}^{2+}$  and 1 MeV  $\text{Cs}^{13+}$  ions was performed to introduce these ion species into the materials to ion fluences of  $2.8 \times 10^{16} \text{ Ag}^{2+}/\text{cm}^2$  (110 dpa in  $\text{Ti}_3\text{SiC}_2$  and 84 dpa in SiC) at 873 K,  $1.0 \times 10^{16} \text{ Au}^{2+}/\text{cm}^2$  (60 dpa in  $\text{Ti}_3\text{SiC}_2$ ) from 230 to 873 K, and  $5.7 \times 10^{16} \text{ Cs}^{13+}/\text{cm}^2$  (239 dpa in  $\text{Ti}_3\text{SiC}_2$ ) at 673 K, respectively. These correspond to the atomic percentages of 3.5 at.% Ag in  $\text{Ti}_3\text{SiC}_2$ , 3.7 at.% Ag in SiC, 0.81 at.% Au in  $\text{Ti}_3\text{SiC}_2$ , and 4.0 at.% Cs in  $\text{Ti}_3\text{SiC}_2$  at their respective profile peak maxima. Rutherford backscattering spectrometry (RBS) was used to measure the depth profiles of the implanted species. It was found that while Ag was immobile in SiC during ion implantation at 873 K, as expected, it underwent outward diffusion in  $\text{Ti}_3\text{SiC}_2$  within the nanocomposite. Further Ag out-diffusion in  $\text{Ti}_3\text{SiC}_2$  at 1073 and 1273 K was also observed, but Ag in SiC remained immobile up to 1273 K for 120 min. An in-situ RBS study of  $\text{Au}^{2+}$  implanted  $\text{Ti}_3\text{SiC}_2$  shows that Au diffusion to the surface started at the implantation temperature of  $\sim 773$  K, followed by a significant Au diffusion in  $\text{Ti}_3\text{SiC}_2$  during implantation at 873 K. Helium ion microscopy (HIM) of the implanted samples suggest that there is different volume swelling between  $\text{Ti}_3\text{SiC}_2$  and residual TiC implanted at 230 K. Studies from micro-beam x-ray diffraction (micro-XRD) indicate a high level of lattice damage or amorphization in  $\text{Ti}_3\text{SiC}_2$  produced at 230 K. Both isothermal and isochronal annealing experiments were conducted for  $\text{Cs}^{13+}$  implanted  $\text{Ti}_3\text{SiC}_2$ . The results show that for 30 min isochronal annealing, there was little Cs diffusion up to 923 K; significant out-diffusion and release occurred at 973 K, followed by more diminishing Cs diffusion and release at higher temperatures up to 1073 K. For isothermal annealing at 1073 K, some Cs diffusion was observed after the first 5 min; considerable out-diffusion and release occurred at 15 min with more Cs loss at 30 min. Cs profile and retention were hardly changed during further annealing up to 120 min. In addition, surface oxidation and decomposition of  $\text{Ti}_3\text{SiC}_2$  occurred during furnace annealing at 1173 K for 30 min under flowing Ar gas conditions.

## **Acknowledgments**

A portion of the research was performed using EMSL, a national scientific user facility sponsored by the DOE's Office of Biological and Environmental Research and located at PNNL. Cesium ion implantation was conducted at the Institute of Modern Physics, Chinese Academy of Sciences. We would like to acknowledge Douglas Conner and Clyde Chamberlin for sample cutting and polishing, Chonghong Zhang and Jie Gou for Cs ion implantation, Tamas Varga for XRD, and Limin Zhang and Amila Dissanayake for assistance in performing some of the experiments.

## Acronyms and Abbreviations

CVD	Chemical Vapor Deposition
dpa	Displacements per Atom
ECR	Electron Cyclotron Resonance
EMSL	Environmental Molecular Sciences Laboratory
FWHM	Full Width at Half Maximum
GIXRD	Grazing-angle Incidence X-ray Diffraction
HIM	Helium Ion Microscopy
IMP	Institute of Modern Physics
MAX	$M_{n+1}AX_n$ with $n = 1, 2,$ or $3$ , where $M$ is an early transition metal, $A$ is mostly elements in group 13 or 14, and $X$ is C or N
Micro-XRD	Micro-beam X-ray Diffraction
NEC	National Electrostatics Corporation
NEET	Nuclear Energy Enabling Technologies
PNNL	Pacific Northwest National Laboratory
RBS/C	Rutherford Backscattering Spectrometry under Channeling condition
SEM	Secondary Electron Microscopy
SRIM03	Stopping and Range of Ions in Matter code, version 2003
TEM	Transmission Electron Microscopy
TOPAS	Total Pattern Analysis Solution
TRISO	Tristructural Isotropic
XRD	X-ray Diffraction
$\alpha_a$	Thermal Expansion Coefficient along $a$ Axis
$\alpha_c$	Thermal Expansion Coefficient along $c$ Axis
$\chi_{\min}$	Minimum Yield
$\kappa_{\text{th}}$	Thermal Conductivity

# Contents

Abstract .....	iv
Summary .....	v
Acknowledgments.....	vi
Acronyms and Abbreviations.....	vii
Figures.....	ix
Tables .....	x
1.0 Introduction.....	1
2.0 Structure and Properties of MAX Phase $Ti_3SiC_2$ .....	2
3.0 Experimental Methods.....	3
3.1 Materials.....	3
3.2 Ion Implantation and Thermal Annealing .....	5
3.3 Sample Characterizations .....	6
4.0 Results and Discussion .....	7
4.1 $Ag^{2+}$ Ion Implanted 6H-SiC, CVD 3C-SiC, and $Ti_3SiC_2/3C-SiC$ .....	7
4.2 $Au^{2+}$ Ion Implanted $Ti_3SiC_2$ .....	8
4.3 $Cs^{13+}$ Ion Implanted $Ti_3SiC_2$ .....	11
5.0 Conclusions.....	13
6.0 References.....	15

## Figures

Figure 1.	Unit cell of $\text{Ti}_3\text{SiC}_2$ : (a) polyhedra of $\text{Ti}_6\text{C}$ separated by Si layers and (b) a close-packed hexagonal structure showing the stacking with the C occupying the octahedral sites within the Ti-Ti layers. ....	2
Figure 2.	Picture of two polycrystalline $\text{Ti}_3\text{SiC}_2/3\text{C-SiC}$ nanocomposite plates ( $3\times 6\times 1\text{ mm}^3$ ), a polycrystalline CVD 3C-SiC disk (8 mm in diameter and 1 mm in thickness) and a 6H-SiC single crystal wafer ( $8\times 8\times 0.3\text{ mm}^3$ ) used in this study.....	4
Figure 3.	XRD pattern of a polycrystalline CVD 3C-SiC with an average crystallite size of 33.4 nm. A small fraction of secondary phase 2H-SiC is likely. ....	4
Figure 4.	XRD pattern of a dual-phase nanocomposite $\text{Ti}_3\text{SiC}_2/3\text{C-SiC}$ with average crystallite sizes of 34 nm for $\text{Ti}_3\text{SiC}_2$ and 23 nm for 3C-SiC. ....	4
Figure 5.	XRD pattern of a polycrystalline $\text{Ti}_3\text{SiC}_2$ plate cut and polished from a hot-pressed bulk ingot (inserted optical image). ....	4
Figure 6.	SRIM03 simulations of the displacement rates and Ag atoms implanted $7^\circ$ off normal in (a) SiC and (b) $\text{Ti}_3\text{SiC}_2$ at ion energy of 400 keV.....	5
Figure 7.	SRIM03 simulation of the displacement rates and Au atoms implanted at normal incidence in $\text{Ti}_3\text{SiC}_2$ at ion energy of 2.0 MeV.....	6
Figure 8.	SRIM03 simulation of the displacement rates and Cs atoms implanted $7^\circ$ off normal in $\text{Ti}_3\text{SiC}_2$ at ion energy of 1.0 MeV. ....	6
Figure 9.	2.0 MeV $\text{He}^+$ RBS/C spectra for a (0001)-oriented 6H-SiC implanted $7^\circ$ off normal with 400 keV $\text{Ag}^{2+}$ at 873 K to $2.8\times 10^{16}$ ions/ $\text{cm}^2$ . Also included are the random and <0001>-aligned spectra from an unimplanted area.....	7
Figure 10.	(a) 2.0 MeV $\text{He}^+$ RBS spectra for (a) a polycrystalline CVD 3C-SiC and (b) a $\text{Ti}_3\text{SiC}_2/3\text{C-SiC}$ nanocomposite implanted $7^\circ$ off normal with 400 keV $\text{Ag}^{2+}$ at 873 K to $2.8\times 10^{16}$ ions/ $\text{cm}^2$ . ....	8
Figure 11.	A sequence of in-situ 3.0 MeV $\text{He}^+$ RBS spectra for a polycrystalline $\text{Ti}_3\text{SiC}_2$ implanted with 2.0 MeV $\text{Au}^{2+}$ at various implantation temperatures to the same ion fluence of $1.0\times 10^{16}$ ions/ $\text{cm}^2$ . ....	9
Figure 12.	A series of HIM images of a polycrystalline $\text{Ti}_3\text{SiC}_2$ before and after 2.0 MeV $\text{Au}^{2+}$ ion implantation at various temperatures to the same ion fluence of $1.0\times 10^{16}$ ions/ $\text{cm}^2$ (field of view: 10 $\mu\text{m}$ ). ....	9
Figure 13.	A sequence of micro-beam GIXRD patterns ( $\omega = 5^\circ$ ) for polycrystalline $\text{Ti}_3\text{SiC}_2$ implanted with 2.0 MeV $\text{Au}^{2+}$ at various implantation temperatures to the same ion fluence of $1.0\times 10^{16}$ ions/ $\text{cm}^2$ . ....	10
Figure 14.	30 min isochronal annealing of a polycrystalline $\text{Ti}_3\text{SiC}_2$ implanted with 1.0 MeV $\text{Cs}^{13+}$ at 673 K to an ion fluence of $5.7\times 10^{16}$ ions/ $\text{cm}^2$ . ....	11
Figure 15.	1073 K isothermal annealing of a polycrystalline $\text{Ti}_3\text{SiC}_2$ implanted with 1.0 MeV $\text{Cs}^{13+}$ at 673 K to an ion fluence of $5.7\times 10^{16}$ ions/ $\text{cm}^2$ . ....	12
Figure 16.	3.0 MeV $\text{He}^+$ RBS/non-RBS spectrum for a polycrystalline $\text{Ti}_3\text{SiC}_2$ implanted with 1.0 MeV $\text{Cs}^{13+}$ at 673 K to an ion fluence of $5.7\times 10^{16}$ ions/ $\text{cm}^2$ and subsequently annealed in furnace at 1173 K for 30 min in flowing Ar gas.....	12

## Tables

Table 1.	Materials, ion implantation and thermal annealing conditions. ....	3
Table 2.	SRIM03 simulation parameters and results. ....	5

# 1.0 Introduction

Silicon carbide (SiC) and SiC/SiC composites have been proposed and tested as a cladding material for nuclear fuels (such as UCO and UO<sub>2</sub>) in the tristructural-isotropic (TRISO)-coated particle design [1-4]. It consists of four layers of surface coatings, including a SiC layer of several to tens of microns in thickness. The SiC layer not only provides the mechanical strength for the fuel particle, but also acts as an impenetrable barrier for fission products, including metallic and gaseous species. The behavior of fission products in the TRISO-coated particles was studied up to 1573 K with high burn-up (up to 10%) [5]. Tests of the post-irradiated TRISO coated fuel particles at accident temperatures of 1973 and 2073 K were also performed [6]. The results show that the irradiated fuel in the pre-heating test has a relatively large fractional release of the excited state <sup>110m</sup>Ag compared to other radionuclides, such as <sup>137</sup>Cs, <sup>154</sup>Eu and <sup>85</sup>Kr. The time-dependent fractional release of <sup>110m</sup>Ag is the highest. Large cracks of the SiC layer was also found after annealing at the extremely high temperatures.

Our early study [7] of Ag diffusivity in both crystalline and amorphized SiC indicated that Ag is immobile in SiC up to 1573 K even in the presence of ion irradiation. The results were confirmed by a number of research groups [8-11]. First-principles calculations [12] suggest that Ag is immobile in the SiC bulk, but becomes mobile on SiC surfaces. The inner surfaces of the interconnected pores and micro-cracks in CVD SiC could provide a faster diffusion path for Ag to reach the surface of the fuel particle. Ag could also evaporate and release in the gas form through the pathway. It is currently believed that micro-cracks and pores in the CVD SiC layer play a key role in the Ag transport. SiC as a cladding material has a number of potential advantages, including good high-temperature corrosion properties, great high-temperature strength, low effective neutron absorption cross section, and good dimensional stability at high temperatures. However, it is brittle, which can promote in-service failure. The material is vulnerable to oxidation under certain conditions and its susceptibility to stress corrosion cracking is not yet clear. It gradually loses strength due to neutron irradiation, affecting its mechanical integrity during service. The cost, joining and chemical stability with the fuel and coolant are also major issues confronting the development of SiC fuel cladding [13].

In order to improve fuel performance and prevent fission products from release, more ductile cladding materials with very low diffusivities of fission products at reactor-relevant high temperatures need to be explored. MAX phases (M<sub>n+1</sub>AX<sub>n</sub> with n = 1, 2, or 3, where M is an early transition metal, A is mostly elements in group 13 or 14, and X is C or N) have a layered, hexagonally close-packed structure. They share outstanding properties of both metals (machinable, ductile, highly thermally conductive, highly radiation-resistant, etc.) and ceramics (elastically stiff, highly corrosion resistant, thermal shock resistant, having a high melting point, etc.). As such, MAX phase materials are considered as hybrids of ceramics and metals. The unique combination of the properties may make them good candidates for use as structural materials in nuclear reactors. Titanium silicon carbide (Ti<sub>3</sub>SiC<sub>2</sub>), the most studied MAX phase to date, has fracture toughness about three times higher than SiC at ambient temperature [14]. The ternary compound has been proposed as a possible fuel-cladding material [15-19]. To the best of our knowledge, there have been no diffusion studies of fission products in Ti<sub>3</sub>SiC<sub>2</sub> or other MAX phases to date. It is of scientific interest and technological importance to investigate and understand the diffusion behavior, especially at elevated temperatures. In this study, fission product surrogates (Ag and Cs) and a noble metal (Au) were introduced into MAX phase Ti<sub>3</sub>SiC<sub>2</sub>, SiC, and a dual-phase nanocomposite of Ti<sub>3</sub>SiC<sub>2</sub>/SiC using ion implantation. The diffusion behavior of the implanted species and structural changes were studied as a function of annealing temperature (isochronal), duration (isothermal) and irradiation status (present or absent) using Rutherford backscattering spectrometry (RBS), x-ray diffraction (XRD) and helium ion microscopy (HIM).

## 2.0 Structure and Properties of MAX Phase $\text{Ti}_3\text{SiC}_2$

Titanium silicon carbide is one of the MAX phases in the group 312, and is the only known Si-containing bulk MAX phase. MAX phases have a hexagonal, layered structure with space group  $P6_3/mmc$  (194), combining  $M_6X$  octahedra with a single intercalating layer A. There are over 60 MAX phases currently known in 3 groups (211, 312 and 413) with different compositions and lattice parameters [14]. MAX phases with new compositions are still being discovered, especially in the group 413. Figure 1 shows the lattice structure of  $\text{Ti}_3\text{SiC}_2$  unit cell [20] with  $a = 0.307$  nm,  $c = 1.767$  nm and a theoretical density of  $4.52$  g/cm<sup>3</sup> [14,21]. The close-packed Ti and Si layers are arranged in the sequence of Ti-Ti-Ti-Si-Ti-Ti-Ti-Si, with C occupying the octahedral sites between the Ti layers, forming  $\text{Ti}_6\text{C}$  polyhedra that are edge sharing. Si atoms are located at the center of trigonal prisms. There are two polymorphs of  $\text{Ti}_3\text{CSi}_2$ , i.e.,  $\alpha$  and  $\beta$  polytypes, with stacking sequences of  $A\gamma B\alpha B\gamma A\beta C\alpha C\beta A\gamma B\alpha B\gamma A$  and  $A\gamma B\alpha B\gamma A\beta C\beta C\beta A\gamma B\alpha B\gamma A$ , respectively, where the capital letters denote Ti layers, low-case letters Si layers, and Greek letters C positions. The only difference between the two polytypes is the Si position in the lattice [19]. Since transformation from  $\alpha$ - to  $\beta$ - $\text{Ti}_3\text{SiC}_2$  does not involve breaking the strong Ti-C bonds, the process has relatively low activation energy. The simulated diffraction patterns of the two polytypes look similar, but can be readily distinguishable by the locations of their 100% reflection peaks ( $2\theta = \sim 39.5^\circ$  for  $\alpha$ - $\text{Ti}_3\text{SiC}_2$  and  $\sim 42.5^\circ$  for  $\beta$ - $\text{Ti}_3\text{SiC}_2$ ) [14]. There is a repeat of two  $\text{Ti}_6\text{C}$  octahedra with an intercalating layer of Si atoms in the  $\text{Ti}_3\text{SiC}_2$  structure (group 312), while MAX phases in groups 211 and 413 have repeats of one and three  $M_6X$  octahedra, respectively.

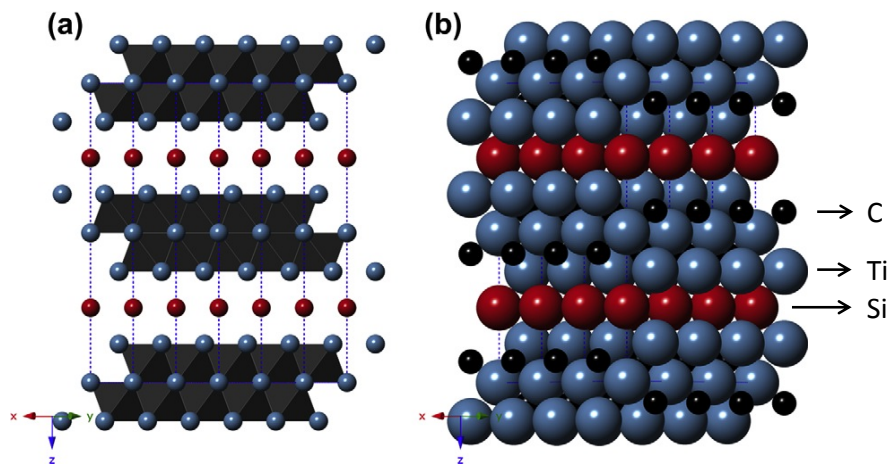


Figure 1. Unit cell of  $\text{Ti}_3\text{SiC}_2$ : (a) polyhedra of  $\text{Ti}_6\text{C}$  separated by Si layers and (b) a close-packed hexagonal structure showing the stacking with the C occupying the octahedral sites within the Ti-Ti layers.

In general, MAX phases, including  $\text{Ti}_3\text{SiC}_2$ , are considered as a hybrid of metals and ceramics because they have both metallic nature of the M-X bonds that are exceptionally strong and the elongated M-A bonds that are relative weak (especially in shear) in the layered structure, resulting in an unusual combination of physical and chemical properties. The ternary compounds are elastically stiff, yet relatively soft and readily machinable. They behave like a “ductile ceramic” with high fracture toughness and good thermal and electrical conductivities. The materials are the only polycrystalline solids that deform by a combination of kink and shear band, together with the delaminations of individual grains. Dislocations in MAX phases multiply and are mobile at room temperature, glide on the basal plane, and are arranged either in arrays or kink boundaries.  $\text{Ti}_3\text{SiC}_2$  combines mechanical anisotropy with thermal

properties that are fairly isotropic ( $\alpha_a = 8.6 \times 10^{-6} \text{ K}^{-1}$  and  $\alpha_c = 9.7 \times 10^{-6} \text{ K}^{-1}$  [22]). It has a thermal conductivity ranging from  $\kappa_{th} = 37 \text{ Wm}^{-1}\text{K}^{-1}$  at 300 K to  $32 \text{ Wm}^{-1}\text{K}^{-1}$  at 1300 K, mostly from electronic contributions. Pure  $\text{Ti}_3\text{SiC}_2$  is thermally stable up to at least 1973 K [14], but decomposes in vacuum between 1273 and 1473 K [23] due to low barriers to Si loss. Polycrystalline  $\text{Ti}_3\text{SiC}_2$  can be readily oxidized in air over the temperature range between 1173 and 1673 K [24], forming an outer layer of pure  $\text{TiO}_2$  (rutile) and an inner layer of mixed  $\text{TiO}_2$  and  $\text{SiO}_2$ . The silica is amorphous at and below 1513 K and becomes a crystalline phase of cristobalite at temperatures higher than 1513 K. Growth of the oxide layers occurs by the inward diffusion of oxygen and the simultaneous outward diffusion of titanium. The oxidation kinetics are initially parabolic and become linear after 30 hr. annealing of polycrystalline  $\text{Ti}_3\text{SiC}_2$  in air at temperatures ranging from 1148 to 1473 K [25]. The overall oxidation reaction for  $\text{Ti}_3\text{SiC}_2$  is:  $\text{Ti}_3\text{SiC}_2 + 6\text{O}_2 = 3\text{TiO}_2 + \text{SiO}_2 + 2\text{CO}_2$ . With the exception of  $\text{HNO}_3$ , MAX phase  $\text{Ti}_3\text{SiC}_2$  has a very low corrosion rate in many of the common acids and  $\text{NaOH}$  at room temperature [26]. It is also resistant to thermal shock [27,28] and creep [29,30], and is tolerant to mechanical damage [14] and irradiation-induced amorphization [16-20,31].

### 3.0 Experimental Methods

#### 3.1 Materials

Samples used in this study include polycrystalline  $\text{Ti}_3\text{SiC}_2$  ( $10 \times 10 \times 1 \text{ mm}^3$ ), dual-phase nanocomposite of  $\text{Ti}_3\text{SiC}_2/3\text{C-SiC}$  ( $3 \times 6 \times 1 \text{ mm}^3$ ) synthesized at PNNL, CVD 3C-SiC (8 mm in diameter and 1 mm in thickness), and single crystal  $\langle 0001 \rangle$ -oriented 6H-SiC ( $8 \times 8 \times 0.3 \text{ mm}^3$ ), as listed in Table 1.

Table 1. Materials, ion implantation and thermal annealing conditions.

Material	Ion	Energy (MeV)	Fluence ( $10^{16}$ ions/cm <sup>2</sup> )	Sample Tilt (Deg.)	Irr. Temp. (K)	Ann. Temp./Time/Environment
$\text{Ti}_3\text{SiC}_2/3\text{C-SiC}$ CVD 3C-SiC 6H-SiC	$\text{Ag}^{2+}$	0.4	2.8	7°	873	1073,1273 K 120 min, Ar
$\text{Ti}_3\text{SiC}_2$	$\text{Au}^{2+}$	2.0	1.0	0°	230,300,373,473, 573,673,773,873	None
$\text{Ti}_3\text{SiC}_2$	$\text{Cs}^{13+}$	1.0	5.7	7°	673	1073 K: 5,15,30,60,120 min, $10^{-6}$ Torr; 30 min: 723,773,823,873, 923,973,1023,1073 K, $10^{-6}$ Torr; 1173 K, 30 min, Ar

The  $\text{Ti}_3\text{SiC}_2/3\text{C-SiC}$ , CVD 3C-SiC and 6H-SiC samples, shown in Figure 2, were obtained from previous projects. The XRD pattern from a symmetric scan based on Cu K $\alpha$  radiation ( $\lambda = 0.154 \text{ nm}$ ) for polycrystalline CVD 3C-SiC is shown in Figures 3. The data suggests that the major phase of the CVD sample is the cubic SiC (3C-SiC) with a very small fraction of the secondary phase, likely 2H-SiC, present in the sample. The average crystallite size of the 3C-SiC is determined to be 33.4 nm. Figure 4 shows the XRD pattern for the nanocomposite  $\text{Ti}_3\text{SiC}_2/3\text{C-SiC}$ . Two major phases in the sample are identified as being cubic phase of SiC and MAX phase  $\alpha\text{-Ti}_3\text{SiC}_2$  with the average crystallite sizes of 23 and 34 nm, respectively. No significant fraction of secondary phases is observed in the nanocomposite.

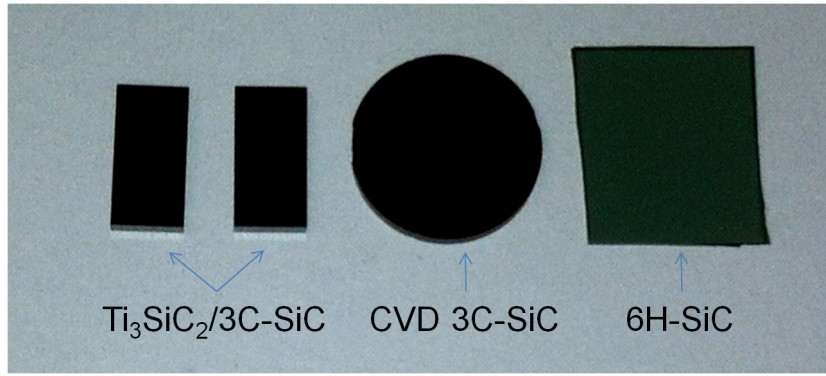


Figure 2. Picture of two polycrystalline  $\text{Ti}_3\text{SiC}_2/3\text{C-SiC}$  nanocomposite plates ( $3 \times 6 \times 1 \text{ mm}^3$ ), a polycrystalline CVD 3C-SiC disk (8 mm in diameter and 1 mm in thickness) and a 6H-SiC single crystal wafer ( $8 \times 8 \times 0.3 \text{ mm}^3$ ) used in this study.

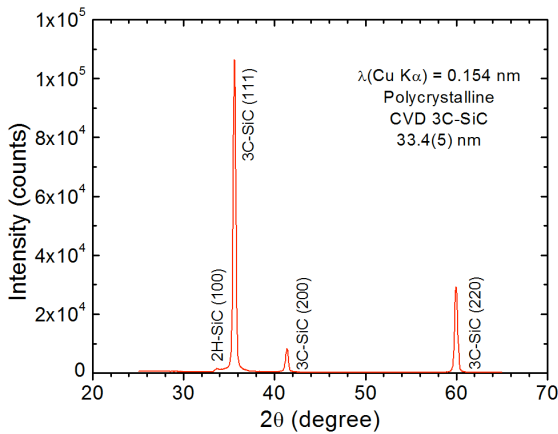


Figure 3. XRD pattern of a polycrystalline CVD 3C-SiC with an average crystallite size of 33.4 nm. A small fraction of secondary phase 2H-SiC is likely.

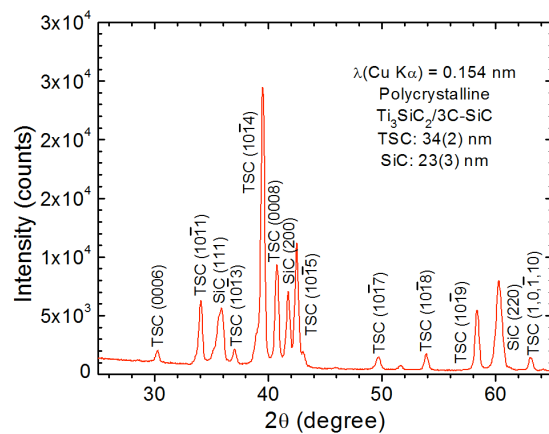


Figure 4. XRD pattern of a dual-phase nanocomposite  $\text{Ti}_3\text{SiC}_2/3\text{C-SiC}$  with average crystallite sizes of 34 nm for  $\text{Ti}_3\text{SiC}_2$  and 23 nm for 3C-SiC.

The 6H-SiC wafer from Cree Inc. had high monocrystalline quality. A hot-pressed bulk ingot of  $\text{Ti}_3\text{SiC}_2$  was purchased from Reade Advanced Materials and was cut into smaller samples, as shown in the inset of Figure 5. The sample surface was ground on diamond laps and silicon carbide sand papers before it was ultrasonically cleaned, rinsed and blow dried. Surface polishing was then performed on a nylon cloth loaded with diamond paste and lapping oil. After cleaning, the samples were further polished using a Struers vibratory polisher for an extended time. The final polishing was performed with a mix of solutions of Struers OPS Colloidal Silica polish and Hydrogen Peroxide. Figure 5 shows the XRD pattern of the  $\text{Ti}_3\text{SiC}_2$  sample. The data indicates that the major phase of the sample is MAX phase  $\alpha\text{-Ti}_3\text{SiC}_2$ . The minor secondary phases include TiC and  $\text{TiSi}_2$ , as indicated in Figure 5.

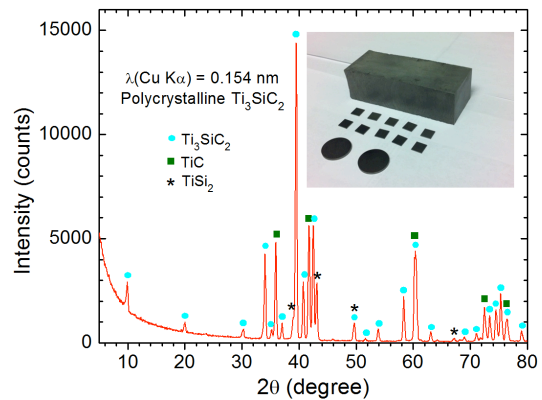


Figure 5. XRD pattern of a polycrystalline  $\text{Ti}_3\text{SiC}_2$  plate cut and polished from a hot-pressed bulk ingot (inserted optical image).

### 3.2 Ion Implantation and Thermal Annealing

Implantation of 400 keV  $^{107}\text{Ag}^{2+}$  in  $\text{Ti}_3\text{SiC}_2/\text{3C-SiC}$ , CVD 3C-SiC and 6H-SiC was conducted  $7^\circ$  off normal to ion fluence of  $2.8 \times 10^{16} \text{ Ag}^{2+}/\text{cm}^2$  at 873 K at INNOVION, California. The results from full-damage cascade SRIM03 simulations [32] for SiC and  $\text{Ti}_3\text{SiC}_2$  are shown in Figure 6 and listed in Table 2. The atomic percentages of the implanted Ag at the profile peak maxima are 3.5 at.% and 3.7 at.% with FWHM of 81 and 74 nm in  $\text{Ti}_3\text{SiC}_2$  and SiC, respectively. The simulations also suggest a dose of 110 dpa at the damage peak (70 nm deep) in  $\text{Ti}_3\text{SiC}_2$  and 84 dpa at the damage peak (87.5 nm deep) in SiC. For dual-phase nanocomposite of  $\text{Ti}_3\text{SiC}_2/\text{3C-SiC}$ , the values are between the two respective limits.

2.0 MeV  $^{197}\text{Au}^{2+}$  ion implantation in  $\text{Ti}_3\text{SiC}_2$  was performed using an NEC 9SDH-2 pelletron 3.0 MV electrostatic tandem accelerator [33] within the Environmental Molecular Sciences Laboratory (EMSL) at the Pacific Northwest National Laboratory (PNNL). The  $\text{Au}^{2+}$  ions were implanted at normal incidence to  $1.0 \times 10^{16} \text{ Au}^{2+}/\text{cm}^2$  at temperatures ranging from 230 to 873 K, corresponding to 60 dpa at the peak maximum (198 nm deep) (Figure 7 and Table 2).

1.0 MeV  $^{133}\text{Cs}^{13+}$  ions were also implanted  $7^\circ$  off normal to  $5.7 \times 10^{16} \text{ Cs}^{13+}/\text{cm}^2$  (239 dpa at peak) at 673 K using a 320 kV high-voltage platform with an ECR-ion-source for highly charged ions at the Institute of Modern Physics (IMP), Chinese Academy of Sciences. According to the SRIM03 simulation results shown in Figures 7 and 8 and listed in Table 2, the atomic percentages of 0.81 at.% Au and 4.0 at.% Cs at the profile peak maxima were estimated at their respective ion fluences. The corresponding FWHM is 133 nm for the Au peak and 162 nm for the Cs peak.

Table 2. SRIM03 simulation parameters and results.

Material	Density (g/cm <sup>3</sup> )	Displ. Energy (eV)	Ion	Energy (MeV)	Fluence (10 <sup>16</sup> ions/cm <sup>2</sup> )	Sample Tilt (Deg.)	Peak Position Displ.; Impl. (nm)	FWHM Displ.; Impl. (nm)	Dose; Ratio (peak dpa; peak at.%)
$\text{Ti}_3\text{SiC}_2$ SiC	4.528 3.21	Ti: 40 Si: 35 C: 20	$\text{Ag}^+$	0.4	2.8	$7^\circ$	70.0; 108 87.5; 123	114; 81 127; 74	110; 3.5% 84; 3.7%
$\text{Ti}_3\text{SiC}_2$	4.528	Ti: 40 Si: 35 C: 20	$\text{Au}^+$	2.0	1.0	$0^\circ$	198; 276	279; 133	60; 0.81%
$\text{Ti}_3\text{SiC}_2$	4.528	Ti: 40 Si: 35 C: 20	$\text{Cs}^+$	1.0	5.7	$7^\circ$	160; 235	259; 162	239; 4.0%

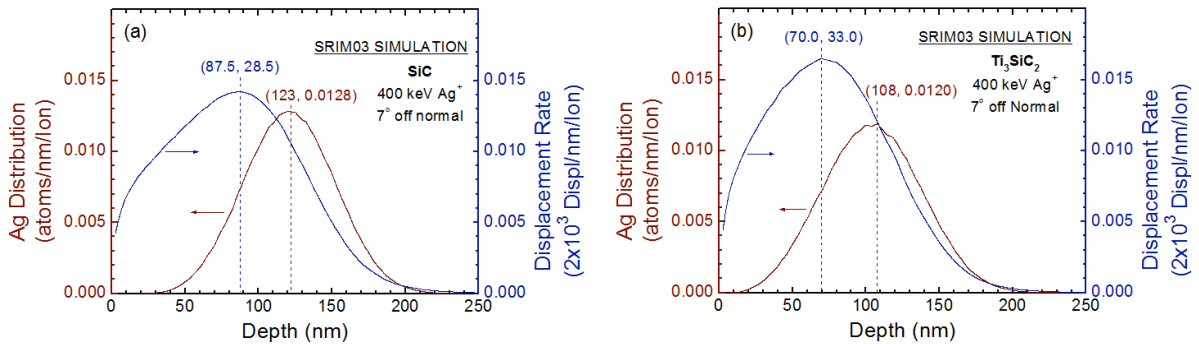


Figure 6. SRIM03 simulations of the displacement rates and Ag atoms implanted  $7^\circ$  off normal in (a) SiC and (b)  $\text{Ti}_3\text{SiC}_2$  at ion energy of 400 keV.

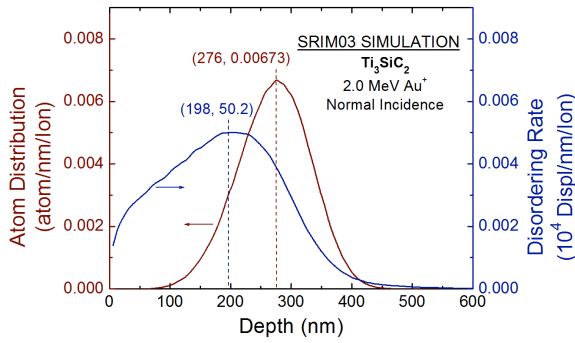


Figure 7. SRIM03 simulation of the displacement rates and Au atoms implanted at normal incidence in  $\text{Ti}_3\text{SiC}_2$  at ion energy of 2.0 MeV.

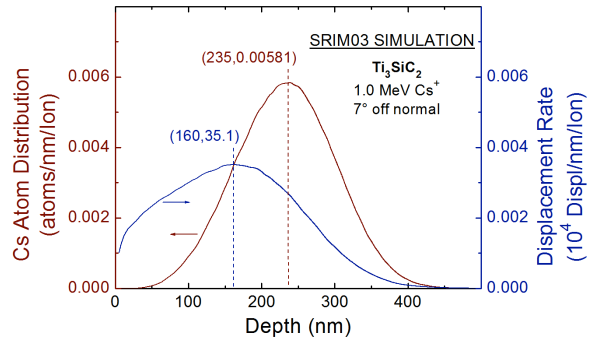


Figure 8. SRIM03 simulation of the displacement rates and Cs atoms implanted  $7^\circ$  off normal in  $\text{Ti}_3\text{SiC}_2$  at ion energy of 1.0 MeV.

Elevated temperatures were used for the ion implantations to minimize lattice damage in  $\text{Ti}_3\text{SiC}_2$  and SiC. Beam rastering systems were employed to achieve uniform implantation. SRIM03 simulations [32] were conducted under the assumption that the threshold displacement energies for Si and C sublattices in SiC were 35 and 20 eV [34], respectively. The same corresponding threshold displacement energies for the Si and C sublattices in  $\text{Ti}_3\text{SiC}_2$  were used, while that for the Ti sublattice was assumed to be 40 eV. The  $\text{Ag}^{2+}$  ion implanted samples at 873 K were furnace annealed at 1073 and 1273 K for 120 min at each temperature under flowing Ar gas conditions. In-situ isothermal annealing in vacuum ( $10^{-6}$  Torr) at 1073 K was performed for the  $\text{Cs}^{13+}$  implanted  $\text{Ti}_3\text{SiC}_2$  for durations from 5 to 120 min; in-situ isochronal annealing in vacuum for 30 min at each temperature was also conducted over the temperature range from 723 to 1073 K. Additional furnace annealing at 1173 K for 30 min was carried out under flowing Ar gas conditions. The ion implantation and thermal annealing conditions are given in Table 1.

### 3.3 Sample Characterizations

Rutherford backscattering spectrometry or non-RBS (resonant RBS) of 2.0 or 3.0 MeV  $\text{He}^+$  ions at a scattering angle of  $150^\circ$  was performed near room temperature to measure the depth profiles of the implanted species in the materials. RBS along the  $\langle 0001 \rangle$  axial channeling direction (RBS/C) in the  $\text{Ag}^{2+}$  implanted 6H-SiC single crystal was used to determine the level of lattice disorder and the substitutional fraction of the implants in the crystal lattice. The experiments were performed at EMSL using the NEC 9SDH-2 pelletron 3.0 MV electrostatic tandem accelerator [33]. Both symmetric scan XRD and GIXRD were conducted using a Philips X'Pert multipurpose diffractometer with a fixed Cu anode ( $\lambda_{\text{Cu}} = 0.154$  nm) operating at 45 kV and 40 mA. Micro-XRD measurements were made with a Rigaku MicroMax 007HF system with a rotating Cr anode ( $\lambda_{\text{Cr}} = 0.229$  nm) and a 2D image plate detector. The RBS/C and micro-XRD measurements were repeated under the same conditions for the annealed samples and the as-implanted samples at different implantation temperatures to study the behavior of implants and structural changes. In addition, the surface morphology of the  $\text{Au}^{2+}$  ion implanted  $\text{Ti}_3\text{SiC}_2$  was examined using HIM under the secondary electron mode at the  $\text{He}^+$  ion energy of 30 keV.

## 4.0 Results and Discussion

### 4.1 Ag<sup>2+</sup> Ion Implanted 6H-SiC, CVD 3C-SiC, and Ti<sub>3</sub>SiC<sub>2</sub>/3C-SiC

2.0 MeV He<sup>+</sup> RBS/C measurements for 6H-SiC before and after Ag<sup>2+</sup> ion implantation were performed at room temperature along the <0001> axis. <sup>107</sup>Ag was used as surrogate for fission product <sup>110m</sup>Ag in this study. The channeling and random spectra from the implanted and unimplanted areas are shown in Figure 9. The depth scales for the Si sublattice and the implanted Ag, shown on the top and inserted axes, respectively, are estimated from the SRIM03 database [32] with the surface energy approximation [35]. The minimum yield,  $\chi_{\min}$ , is ~2.4%, which is determined by the ratio of the integrated yields of the channeling to random spectra of the pristine 6H-SiC in a narrow channel window at the surface. The small value indicates that the single crystal had high crystalline quality prior to ion implantation. The defect concentration in 6H-SiC is respectively defined by the yields of the random and channeling spectra from the unimplanted area, corresponding to amorphous (100%) and essentially defect-free (0%) states. An apparent damage peak is produced as a result of the ion implantation. A rough estimation of the Si defect concentration at the peak maximum (~175 nm deep) based on a linear background approximation [36] leads to a value of 60%. The data suggests that the material is not completely amorphized throughout the entire thickness of the implantation layer. It is interesting to note that the damage peak from implantation at 873 K is much deeper (~175 nm) than SRIM03 prediction (~87.5 nm) with the simulation performed at 0 K. This is primarily due to the migration of Si interstitials during Ag<sup>2+</sup> ion irradiation at 873 K, as has been observed before [7]. The peak FWHM also increases from ~127 nm (SRIM03) to ~150 nm (RBS/C). The Ag peak in Figure 9 shows a Gaussian distribution and is well resolved from the SiC spectrum. The observed Ag peak position (112 nm) and FWHM width (95 nm) are reasonably consistent with the SRIM03 predictions (Figure 6a and Table 2), considering the inaccuracy of the electronic stopping powers in the SRIM03 database, especially for slow heavy ions, including Ag ions at energies of hundreds of keV and lower. The results suggest that noticeable Ag diffusion did not occur during implantation in 6H-SiC at 873 K. This is an expected result and is consistent with our previous observations of immobile Ag in SiC below a temperature of 1573 K [7]. In addition, according to Ag peak intensities from the channeling and random spectra, it can be deduced that ~20 % of the implanted Ag atoms are on the substitutional sites in the 6H-SiC crystal structure, as observed from <0001> axis.

Figures 10a and 10b show the RBS spectra for the Ag<sup>2+</sup> ion as-implanted CVD 3C-SiC and Ti<sub>3</sub>SiC<sub>2</sub>/3C-SiC nanocomposite, respectively. From Figure 10a, Ag diffusion did not occur during implantation in the polycrystalline CVD 3C-SiC at 873 K, indicating that the grain boundaries in the sample did not provide a faster path for Ag diffusion at the elevated temperature. The result agrees well with our previous observation [7] that suggests that Ag is immobile in both crystalline and amorphous

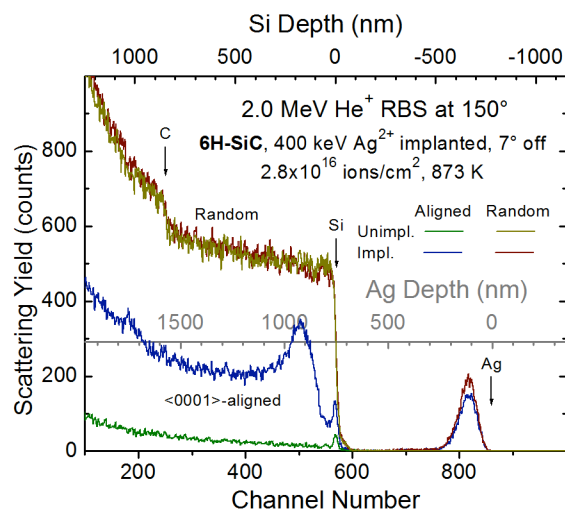


Figure 9. 2.0 MeV He<sup>+</sup> RBS/C spectra for a (0001)-oriented 6H-SiC implanted 7° off normal with 400 keV Ag<sup>2+</sup> at 873 K to 2.8×10<sup>16</sup> ions/cm<sup>2</sup>. Also included are the random and <0001>-aligned spectra from an unimplanted area.

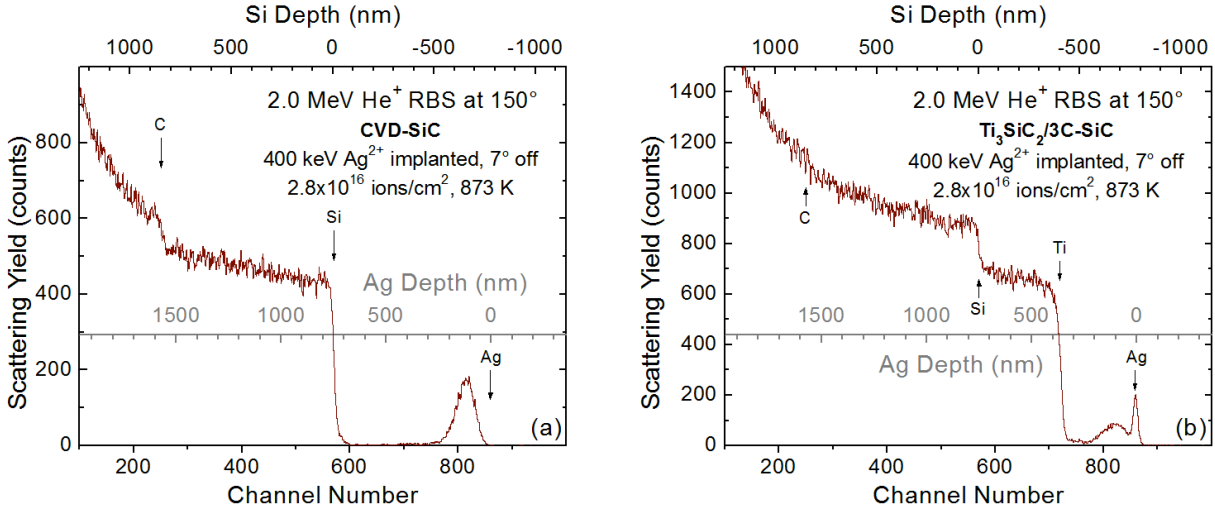


Figure 10. (a) 2.0 MeV He<sup>+</sup> RBS spectra for (a) a polycrystalline CVD 3C-SiC and (b) a Ti<sub>3</sub>SiC<sub>2</sub>/3C-SiC nanocomposite implanted 7° off normal with 400 keV Ag<sup>2+</sup> at 873 K to 2.8 × 10<sup>16</sup> ions/cm<sup>2</sup>.

SiC below 1573 K. The Si and Ag depth scales in Figure 10b are assumed to be about the same as in pure SiC. In the Ag<sup>2+</sup> implanted nanocomposite Ti<sub>3</sub>SiC<sub>2</sub>/3C-SiC, Ag profile consists of two convoluted peaks: a broad peak and a sharper peak. The broad peak corresponds to immobile Ag in 3C-SiC, while the sharper peak is due to the Ag accumulation on the sample surface as a result of Ag outward diffusion in Ti<sub>3</sub>SiC<sub>2</sub> within the nanocomposite during ion implantation at 873 K. Similar results for the Ag diffusion in Ti<sub>3</sub>SiC<sub>2</sub> at 873 K have never been reported in the literature to the best of our knowledge. It remains to be further investigated to develop the diffusion mechanisms in MAX phases and understand the roles of grain boundaries as well.

After furnace annealing of the implanted nanocomposite at 1073 K in flowing Ar gas for 120 min, a surface layer of ~150 nm in thickness on the sample surface was formed. This layer could originate from the deposition of a contaminant element with a similar atomic number to Si, such as Al from the furnace. The same layer on the CVD 3C-SiC was also observed as a result of the same annealing. Some oxygen concentration was also found in the surface layer. During the thermal annealing, further Ag diffusion and accumulation at the newly formed interface were observed. Subsequent annealing at 1273 K for 120 min led to more extensive Ag out-diffusion and release. In addition, the thickness of the surface layer was slightly reduced with some C concentration. In contrast, Ag was observed to be immobile in SiC under the thermal annealing conditions up to the highest temperature applied (1273 K).

## 4.2 Au<sup>2+</sup> Ion Implanted Ti<sub>3</sub>SiC<sub>2</sub>

While Ag<sup>2+</sup> ion implantation was not performed in Ti<sub>3</sub>SiC<sub>2</sub> due to a lack of samples at the time, the experiments on the dual-phase nanocomposite Ti<sub>3</sub>SiC<sub>2</sub>/3C-SiC suggested Ag outward diffusion in Ti<sub>3</sub>SiC<sub>2</sub> during ion implantation at 873 K, as discussed above. Similar to noble metal Ag that does not form chemical bonds with the atoms in the host, an in-situ study of Au diffusion in polycrystalline Ti<sub>3</sub>SiC<sub>2</sub> was conducted as a function of implantation temperature. There were two samples of high-T (873, 773, 673 and 573 K) and low-T (473, 373, 300, and 230 K), each of which had four equal areas for implantation. A sequence of 2.0 MeV Au<sup>2+</sup> ion implantations was conducted at normal incidence to the same ion fluence of 1.0 × 10<sup>16</sup> Au<sup>2+</sup>/cm<sup>2</sup> in each area in order of decreasing temperature starting from 873 to 573 K for the high-T sample and from 473 to 230 K for the low-T sample to minimize or avoid post-implantation thermal annealing effects. Each implantation took 35 – 40 min for the high-T sample and ~24 min for the

low-T sample except for the 230 K area that took 90 min for implantation. The implanted samples were subsequently analyzed in situ near room temperature using 3.0 MeV He<sup>+</sup> RBS. The higher He<sup>+</sup> ion energy was selected to resolve the peak of the implanted Au from the host Ti<sub>3</sub>SiC<sub>2</sub> in the RBS spectrum. The RBS data are shown in Figure 11, with elements Au, Ti and Si on the sample surface indicated by arrows. The two vertical dashed lines show the depth region of the implanted Au and the horizontal dotted lines represent the shifted axes for the RBS spectra. From Figure 11, the Au peak position, width and shape do not change up to 673 K, suggesting that observable Au diffusion in Ti<sub>3</sub>SiC<sub>2</sub> does not occur up to this temperature. The Au atoms appear to start diffusing in Ti<sub>3</sub>SiC<sub>2</sub> during implantation at 773 K, where the peak becomes slightly broader, but its position remains unchanged. There is an extensive Au out-diffusion in Ti<sub>3</sub>SiC<sub>2</sub> during implantation at 873 K. Au accumulation on the surface is clearly visible. The result is similar to the extensive Ag outward diffusion observed in the dual-phase nanocomposite of Ti<sub>3</sub>SiC<sub>2</sub>/3C-SiC during implantation at 873 K (Figure 10b). The RBS spectra at smaller channels (data not shown) does not indicate oxygen presence, suggesting that the material was not decomposed, nor oxidized in vacuum (10<sup>-6</sup> Torr) during the ion implantation up to the highest temperature (873 K) in this in-situ experiment.

The surfaces of the Ti<sub>3</sub>SiC<sub>2</sub> samples implanted with Au<sup>2+</sup> ions at various temperatures, together with an unimplanted sample, were also examined using HIM under the secondary electron mode. The images for all the samples are shown in Figure 12 with the same field of view (10 μm). The unimplanted sample (Figure 12a) exhibits a flat surface with a sharp

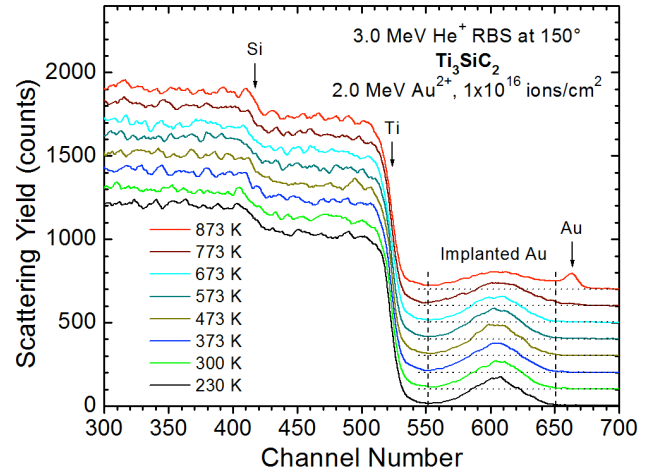


Figure 11. A sequence of in-situ 3.0 MeV He<sup>+</sup> RBS spectra for a polycrystalline Ti<sub>3</sub>SiC<sub>2</sub> implanted with 2.0 MeV Au<sup>2+</sup> at various implantation temperatures to the same ion fluence of 1.0×10<sup>16</sup> ions/cm<sup>2</sup>.

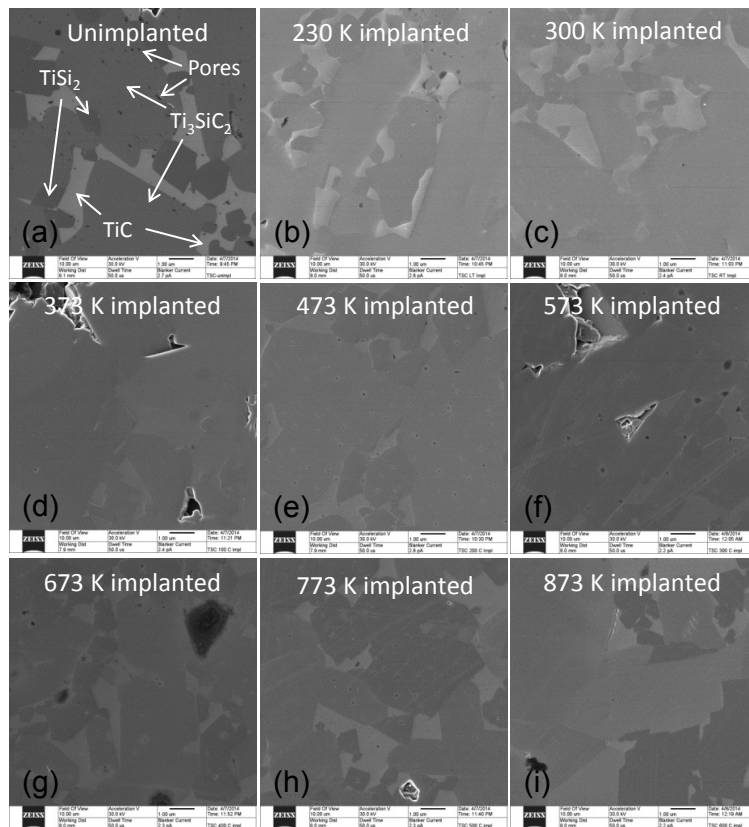


Figure 12. A series of HIM images of a polycrystalline Ti<sub>3</sub>SiC<sub>2</sub> before and after 2.0 MeV Au<sup>2+</sup> ion implantation at various temperatures to the same ion fluence of 1.0×10<sup>16</sup> ions/cm<sup>2</sup> (field of view: 10 μm).

contrast for the grains and pores. The large grains are  $\text{Ti}_3\text{SiC}_2$ , the major phase of the material as indicated by the XRD results in Figure 5. The smaller, darker and brighter particles are  $\text{TiSi}_2$  and  $\text{TiC}$ , respectively, as indicated by arrows in Figure 12a based on previous secondary electron microscopy (SEM) studies [15,16]. The dark dots are pores that do not show preferred locations in the microstructure. The 230 K implanted sample (Figure 12b) appears to exhibit an uneven surface probably due to different volume swelling between  $\text{Ti}_3\text{SiC}_2$  and  $\text{TiC}$ . This effect has not been reported in the literature, and certainly warrants further investigations for better understanding. Apparent fractures or micro-cracks are not observed in the implanted sample. Optically, the surface of this sample has an apparent change in the reflectivity of the visible light, while the rest of the implanted samples do not. The extent of volume swelling may be associated with the residual defect concentration in the microstructure. Different compositions can have different disordering rates and simultaneous defect recovery efficiencies during ion implantation. It is generally expected that ion implantation at a higher temperature leads to a lower residual defect concentration, if the defect concentration is not in a saturation regime. The possible swelling effect is also visible at 300 K (Figure 12c), but becomes less pronounced. The contrast gradually fades out with increasing temperature (Figures 12d to 12i). The phenomena are consistent with a previous observation of  $\text{Au}^+$  ion irradiated  $\text{Ti}_3\text{SiC}_2$  [16], where swelling of  $\text{Ti}_3\text{SiC}_2$  was determined by the step height method to be 2.2% for a dose of 4.3 dpa at room temperature and was attributed to an increase in lattice parameter  $c$  [19].

In addition, micro-GIXRD at  $\omega = 5^\circ$  for the  $\text{Au}^{2+}$  implanted samples was performed using Cr  $K_\alpha$  x-rays ( $\lambda = 0.229$  nm). The data are shown in Figure 13 with vertical offsets for clarity. The path length for the x-rays in  $\text{Ti}_3\text{SiC}_2$  to attenuate its initial intensity to 10% and 50% is estimated to be 15 and 4.5  $\mu\text{m}$ , respectively. For  $\omega = 5^\circ$ , the penetration depth (perpendicular to the sample surface) of the incident pathway corresponds to 1300 and 390 nm. Since the implantation damage band may be extended to a depth of  $\sim 300$  nm or slightly deeper according to SRIM03 full-cascade simulation (Figure 7), the data in Figure 13 has considerable contributions from the unimplanted material. Micro-XRD at  $\omega = 2^\circ$  was also attempted for comparison, but the reflection intensity was too small to show distinct diffraction patterns in a relatively high background within a reasonable data collection time (data not shown). From Figure 13, the micro-GIXRD data exhibit a similar pattern to that in Figure 5, but show a formed secondary phase of  $\text{SiC}$  at 873 K. The diffraction peaks, such as the 100% peak located at  $2\theta \approx 60^\circ$ , become stronger and sharper with increasing implantation temperature starting from 473 K. The results suggest that the  $\text{Ti}_3\text{SiC}_2$  grains have less residual damage produced at higher temperatures during ion irradiation, as generally expected. For a dimension of a few nanometers,  $\text{Ti}_3\text{SiC}_2$  grains could grow to larger sizes with increasing dose, as have been observed for other compositions, such as  $\text{SiC}$  [37],  $\text{ZrO}_2$  [38] and  $\text{Fe}_3\text{O}_4$  [39]. At  $2\theta \approx 133^\circ$ , the diffraction peaks from  $\text{Ti}_3\text{SiC}_2$  are relatively weak for implantation temperatures ranging from 230 to 473 K. This is an indication of the possible formation of highly disordered lattice or amorphized state at the sample surface due to ion implantation, especially at 230 K. The results are in good

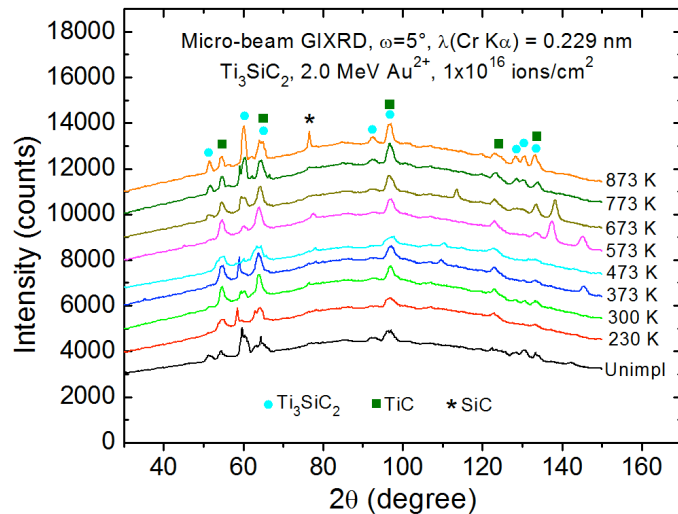


Figure 13. A sequence of micro-beam GIXRD patterns ( $\omega = 5^\circ$ ) for polycrystalline  $\text{Ti}_3\text{SiC}_2$  implanted with 2.0 MeV  $\text{Au}^{2+}$  at various implantation temperatures to the same ion fluence of  $1.0 \times 10^{16}$  ions/cm $^2$ .

agreement with a previous report [17] that showed heavy lattice damage in the structure of Au ion irradiated  $\text{Ti}_3\text{SiC}_2$  through nuclear interactions. High-resolution transmission electron microscopy (TEM) is needed for further studies of the microstructures in the  $\text{Au}^{2+}$  ion implanted samples.

### 4.3 $\text{Cs}^{13+}$ Ion Implanted $\text{Ti}_3\text{SiC}_2$

The stable isotope  $^{133}\text{Cs}$  was implanted as a fission surrogate for  $^{137}\text{Cs}$  to study its diffusion behavior in MAX phase  $\text{Ti}_3\text{SiC}_2$ . The ion implantation was performed  $7^\circ$  off normal with 1.0 MeV  $\text{Cs}^{13+}$  at 673 K to an ion fluence of  $5.7 \times 10^{16}$  ions/cm<sup>2</sup>. 3.0 MeV  $\text{He}^+$  ion RBS was used to measure the Cs depth profile in the as-implanted sample. Both isochronal and isothermal annealing experiments were followed to study Cs diffusion as a function of annealing temperature and duration using in-situ RBS method. The data for the 30-min isochronal annealing at temperatures from 723 to 1073 K are shown in Figure 14, which includes the Cs, Ti and Si spectra to study their evolutions. Also included in the figure is the data for the as-implanted sample at 673 K. The Cs peaks are zoomed in by a factor of 3 for clarity. Apparently, the RBS spectra of  $\text{Ti}_3\text{SiC}_2$  did not change under the implantation conditions, suggesting that the material composition remained the same. In

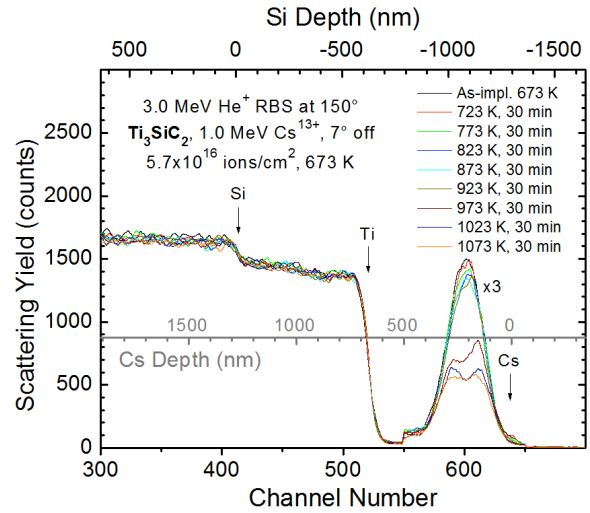


Figure 14. 30 min isochronal annealing of a polycrystalline  $\text{Ti}_3\text{SiC}_2$  implanted with 1.0 MeV  $\text{Cs}^{13+}$  at 673 K to an ion fluence of  $5.7 \times 10^{16}$  ions/cm<sup>2</sup>.

In all cases, the Cs peaks in the spectra are well resolved and located in a low-background region. Compared to SRIM03 prediction in Figure 8, the measured depth profile of Cs in as-implanted  $\text{Ti}_3\text{SiC}_2$  shows similar peak position (208 vs. 235 nm) and FWHM (197 vs. 162 nm), indicating that Cs is not very mobile in  $\text{Ti}_3\text{SiC}_2$  during implantation at 673 K. The peak position, FWHM and shape of the implanted Cs hardly changed after thermal annealing up to 923 K. However, further annealing at 973 K leads to an abrupt change in the peak shape and reduction in intensity. The original Gaussian peak becomes two convoluted peaks with the stronger one closer to the surface, indicating that Cs in MAX phase  $\text{Ti}_3\text{SiC}_2$  diffuses towards the surface at 973 K. Cs did not accumulate on the surface at 973 K, but likely evaporated to vacuum ( $10^{-6}$  Torr) during thermal annealing. About 36% of Cs in  $\text{Ti}_3\text{SiC}_2$  was released based on the reduction in the peak intensity. This behavior is consistent with Cs diffusion and release from SiC at much higher temperatures ( $\sim 1473$  K and above) [40,41]. Unlike Ag and Au in  $\text{Ti}_3\text{SiC}_2$  during ion implantation at 873 K, the temperature for significant Cs diffusion is  $\sim 100$  K higher without evidence of Cs surface accumulation. While surface accumulation depends on chemical bonding and temperature, the increase in temperature is not a big surprise because thermal processes usually take place at lower temperatures when ion irradiation is present. In fact, ion irradiation can enhance diffusion processes through various mechanisms, including ionization-enhanced diffusion mechanism, Bourgoin mechanism, energy-release mechanism and recoil mechanism [42]. Further annealing of the sample at 1023 and 1073 K resulted in diminishing diffusion and loss of Cs, as shown in Figure 14. At the end of the thermal annealing at 1073 K for 30 min, about 50% Cs was released from the implanted  $\text{Ti}_3\text{SiC}_2$ .

Isothermal annealing at 1073 K was performed in vacuum ( $10^{-6}$  Torr) for durations ranging from 5 to 120 min. The in-situ RBS data are shown in Figure 15. The as-implanted sample shows a small peak that is barely seen in Figure 14, which could originate from some surface Cs. There is a small change in the Cs

depth profile after 5 min annealing. It appears that the Cs tends to diffuse towards the surface, but accumulation of Cs on the surface is not evident, which is consistent with the data in Figure 14. The overall reduction in the peak intensity or Cs loss is ~10% at 5 min. A more significant Cs loss of ~30% relative to the total implanted Cs occurred at 15 min, followed by a total Cs loss of ~40% at 30 min, which is statistically not very different from the percentage (~50%) of Cs released after 30 min isochronal annealing at 1073 K (Figure 14). Also similar is the shape of the Cs profile that consists of two convoluted peaks. Further annealing for longer durations up to 120 min does not lead to a significant change in the Cs depth profile.

The Cs<sup>13+</sup> ion implanted Ti<sub>3</sub>SiC<sub>2</sub> sample was also annealed in a furnace at 1173 K for 30 min with flowing Ar gas. The thermal annealing was performed with a ramp-up time of 120 min. The sample was taken out of the furnace at 390 K after 14 hr. cooling to expose to the ambient air. The data from 3.0 MeV He<sup>+</sup> ion RBS/non-RBS measurement on the annealed sample is shown in Figure 16. There is an oxygen peak at the surface from the strong <sup>16</sup>O(α,α)<sup>16</sup>O resonance centered at E = 3.03 MeV [36,43], indicating that the sample surface was oxidized. In spite of flowing Ar gas during thermal annealing, there was obviously also oxygen partial pressure in the furnace tube that could react with the hot Ti<sub>3</sub>SiC<sub>2</sub> surface. The result suggests that MAX phase Ti<sub>3</sub>SiC<sub>2</sub> is susceptible to oxidation at 1173 K. From Figure 16, there is a high Ti concentration starting from the surface. The overall RBS spectrum suggests that the sample surface contains mainly titanium oxide.

The low-yield Si spectrum cannot be resolved from the much higher-yield Ti spectrum in the depth region of Ti concentration transition from mainly titanium oxide to unaffected Ti<sub>3</sub>SiC<sub>2</sub>, as indicated in Figure 16. It is worthwhile to note that previous oxidation studies of MAX phase Ti<sub>3</sub>SiC<sub>2</sub> [24,25] showed the formation of an outer pure TiO<sub>2</sub> (rutile) layer and an inner mixed layer comprised of TiO<sub>2</sub> + SiO<sub>2</sub> (silica) on surface annealed in air at 1373 K for 360 hrs. It was attributed to an inward diffusion of oxygen and a simultaneous outward diffusion of titanium in TiO<sub>2</sub>, while Si atoms were oxidized in situ [14]. Bellucci, et al. [44] presented evidence that the oxidation started with O ions diffusing through TiO<sub>2</sub> layer at the TiC/TiO<sub>2</sub> interface, substituting for C and releasing C as an interstitial that then diffused through the TiO<sub>2</sub> layer and was ultimately oxidized on the TiO<sub>2</sub> surface. As a result of the material decomposition and oxidation, the Cs was no longer in the MAX phase of Ti<sub>3</sub>SiC<sub>2</sub> and diffusion behavior could become very different. This could be an interesting topic for future studies.

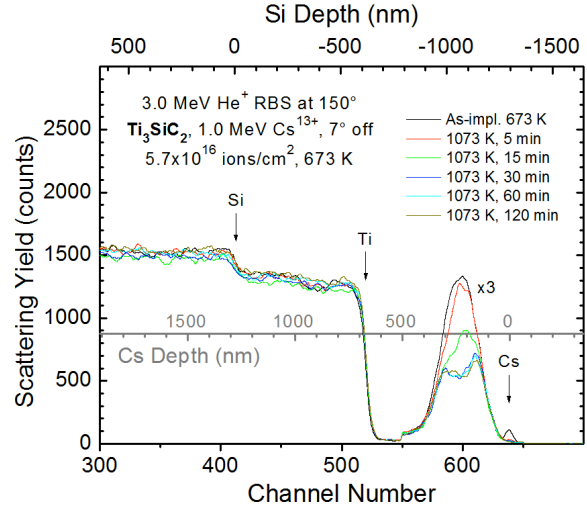


Figure 15. 1073 K isothermal annealing of a polycrystalline Ti<sub>3</sub>SiC<sub>2</sub> implanted with 1.0 MeV Cs<sup>13+</sup> at 673 K to an ion fluence of 5.7×10<sup>16</sup> ions/cm<sup>2</sup>.

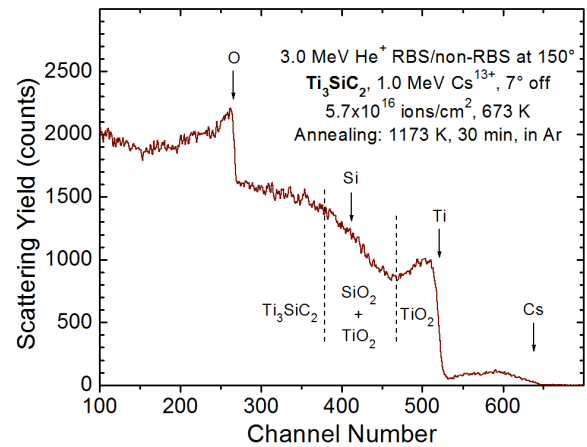


Figure 16. 3.0 MeV He<sup>+</sup> RBS/non-RBS spectrum for a polycrystalline Ti<sub>3</sub>SiC<sub>2</sub> implanted with 1.0 MeV Cs<sup>13+</sup> at 673 K to an ion fluence of 5.7×10<sup>16</sup> ions/cm<sup>2</sup> and subsequently annealed in furnace at 1173 K for 30 min in flowing Ar gas.

## 5.0 Conclusions

Implantation of 400 keV  $\text{Ag}^{2+}$ , 2 MeV  $\text{Au}^{2+}$  and 1 MeV  $\text{Cs}^{13+}$  ions were performed to ion fluences of  $2.8 \times 10^{16} \text{ Ag}^{2+}/\text{cm}^2$  (110 dpa for  $\text{Ti}_3\text{SiC}_2$  and 84 dpa for SiC) in a dual-phase nanocomposite of  $\text{Ti}_3\text{SiC}_2/3\text{C-SiC}$ , polycrystalline CVD 3C-SiC, and single crystal 6H-SiC at 873 K,  $1.0 \times 10^{16} \text{ Au}^{2+}/\text{cm}^2$  (60 dpa) in polycrystalline  $\text{Ti}_3\text{SiC}_2$  from 230 to 873 K, and  $5.7 \times 10^{16} \text{ Cs}^{13+}/\text{cm}^2$  (239 dpa) in polycrystalline  $\text{Ti}_3\text{SiC}_2$  at 673 K, respectively. The  $\text{Ag}^{2+}$  ion implanted nanocomposite and SiC were furnace annealed at 1073 and 1273 K for 120 min at each temperature in flowing Ar gas environment. Both isochronal and isothermal annealing experiments were performed for the  $\text{Cs}^{13+}$  implanted  $\text{Ti}_3\text{SiC}_2$  up to 1073 K and duration of 120 min. Additional furnace annealing was conducted at 1173 K for 30 min. The implanted and annealed samples were characterized using RBS at room temperature. In-situ RBS measurements near room temperature were made for  $\text{Ti}_3\text{SiC}_2$  implanted with  $\text{Au}^{2+}$  ions at temperatures ranging from 230 to 873 K. In addition, HIM and micro-XRD were also used to study the microstructures, phases and implantation damage in  $\text{Au}^{2+}$  ion implanted samples. The experimental results from this study are summarized below:

### 1. $\text{Ag}^{2+}$ ion implanted $\text{Ti}_3\text{SiC}_2/3\text{C-SiC}$ dual-phase nanocomposite:

- Ag is immobile in SiC up to the highest temperature (1273 K) applied in this study. However, there is a significant outward diffusion of Ag in the MAX phase  $\text{Ti}_3\text{SiC}_2$  within the dual-phase nanocomposite of  $\text{Ti}_3\text{SiC}_2/3\text{C-SiC}$  during  $\text{Ag}^{2+}$  ion implantation at 873 K. Accumulation of the diffusive Ag on the surface is observed.
- Post-irradiation furnace annealing at 1073 K in Ar for 120 min led to further Ag outward diffusion; at 1273 K, more extensive Ag out-diffusion and release were observed.

### 2. $\text{Au}^{2+}$ ion implanted polycrystalline $\text{Ti}_3\text{SiC}_2$ :

- The Au atoms appear to start diffusing in  $\text{Ti}_3\text{SiC}_2$  during implantation at 773 K. There is an extensive Au out-diffusion in  $\text{Ti}_3\text{SiC}_2$  during implantation at 873 K. Au accumulation on the surface at 873 K is observed.
- The 230 K implanted sample appears to exhibit different volume swelling between  $\text{Ti}_3\text{SiC}_2$  and residual TiC. The swelling effect is still visible at 300 K, but becomes less pronounced. The contrast gradually fades out with increasing temperature.
- A secondary SiC phase is present at 873 K. There is less residual damage produced at higher temperatures during ion irradiation. A highly disordered lattice or an amorphized state near the  $\text{Ti}_3\text{SiC}_2$  surface is likely resulted from  $\text{Au}^{2+}$  ion implantation of  $\text{Ti}_3\text{SiC}_2$  at 230 K.

### 3. $\text{Cs}^{13+}$ ion implanted polycrystalline $\text{Ti}_3\text{SiC}_2$ :

- Cs appears to be not very mobile in  $\text{Ti}_3\text{SiC}_2$  during implantation at 673 K and during post-implantation thermal annealing up to 923 K.
- There is significant Cs diffusion towards the surface at 973 K with ~36% Cs released to vacuum ( $10^{-6}$  Torr) after 30 min annealing; no evidence of Cs accumulation on the surface at 973 K is found.
- Further annealing at 1023 and 1073 K resulted in diminishing diffusion and loss of Cs. About 50% Cs was released from the implanted  $\text{Ti}_3\text{SiC}_2$  at 1073 K for 30 min.
- After first 5 min annealing at 1073 K, Cs tends to diffuse towards the surface, but accumulation of Cs on the surface is not observed. The overall Cs loss is ~10%.
- A more significant Cs loss of ~30% occurred at 15 min, followed by a total Cs loss of ~40% at 30 min. Further annealing for longer durations up to 120 min did not lead to a significant change in the Cs depth profile in  $\text{Ti}_3\text{SiC}_2$ .

- MAX phase  $\text{Ti}_3\text{SiC}_2$  is susceptible to oxidation and decomposition at 1173 K.
- After furnace annealing at 1173 K for 30 min in flowing Ar gas, the  $\text{Ti}_3\text{SiC}_2$  surface turned to be mainly titanium oxide. The observation is consistent with a previous report that showed an outer pure  $\text{TiO}_2$  (rutile) layer and an inner layer comprising  $\text{TiO}_2$  and  $\text{SiO}_2$  (silica) after annealing in air at 1373 K for 360 hrs.

The results from this study indicate that diffusion of Ag, Au and Cs in MAX phase  $\text{Ti}_3\text{SiC}_2$  occurs at relatively low temperatures (773 – 973 K). Surface oxidation of  $\text{Ti}_3\text{SiC}_2$  takes place at slightly higher temperatures (1073 – 1173 K). Because these temperatures are still low for the advanced high-temperature reactor designs, this study may suggest caution in using  $\text{Ti}_3\text{SiC}_2$  as a fuel cladding material for advanced nuclear reactors operating at very high temperatures. Further studies of impurity transport in the related materials may be warranted based on the results of this study.

## 6.0 References

- [1] K. Minato, H. Kikuchi, K. Fukuda, N. Suzuki, H. Tomimoto, N. Kitamura, and M. Kaneko, *Nuclear Technol.* **106**, 342 (1994).
- [2] P. A. Lessing and R. J. Heaps, *Nuclear Technol.* **108**, 207 (1994).
- [3] K. Minato, H. Kikuchi, K. Fukuda, N. Suzuki, H. Tomimoto, N. Kitamura, and M. Kaneko, *Nuclear Technol.* **111**, 260 (1995).
- [4] B. G. Kim, Y. Choi, J. W. Lee, Y. W. Lee, D. S. Sohn, and G. M. Kim, *J. Nucl. Mater.* **281**, 163 (2000).
- [5] M. Barrachin, R. Dubourg, S. de Groot, M. P. Kissane, and K. Bakker, *J. Nucl. Mater.* **415**, 104 (2011).
- [6] K. Minato, K. Sawa, T. Koya, T. Tomita, A. Ishikawa, C. A. Baldwin, W. A. Gabbard, and C. M. Malone, *Nuclear Technol.* **131**, 36 (2000).
- [7] W. Jiang, W. J. Weber, V. Shutthanandan, L. Li, and S. Thevuthasan, *Nucl. Instrum. Meth. Phys. Res. B* **219-220**, 642 (2004).
- [8] H. J. MacLean, R. G. Ballinger, L. E. Kolaya, S. A. Simonson, N. Lewis, and M. E. Hanson, *J. Nucl. Mater.* **357**, 31 (2006).
- [9] E. Friedland, J. B. Malherbe, N. G. van der Berg, T. Hlatshwayo, A. J. Botha, E. Wendler, and W. Wesch, *J. Nucl. Mater.* **389**, 326 (2009).
- [10] E. Friedland, N. G. van der Berg, J. B. Malherbe, J. J. Hancke, J. Barry, E. Wendler, and W. Wesch, *J. Nucl. Mater.* **410**, 24 (2011).
- [11] T. T. Hlatshwayo, J. B. Malherbe, N. G. van der Berg, L. C. Prinsloo, A. J. Botha, E. Wendler, and W. Wesch, *Nucl. Instrum. Meth. Phys. Res. B* **274**, 120 (2012).
- [12] H. Y. Xiao, Y. Zhang, L. L. Snead, V. Shutthanandan, H. Z. Xue, and W. J. Weber, *J. Nucl. Mater.* **420**, 123 (2012).
- [13] C. R. F. Azevedo, *Eng. Failure Anal.* **18**, 1943 (2011).
- [14] M. W. Barsoum, *MAX Phases: Properties of Machinable Ternary Carbides and Nitrides*, Wiley-VCH Verlag GmbH, 2013.
- [15] J. C. Nappé, I. Monnet, F. Audubert, Ph. Grosseau, M. Beauvy, and M. Benabdesselam, *Nucl. Instrum. Meth. Phys. Res. B* **270**, 36 (2012).
- [16] J. C. Nappé, C. Maurice, Ph. Grosseau, F. Audubert, L. Thomé, B. Guilhot, M. Beauvy, and M. Benabdesselam, *J. Euro. Ceram. Soc.* **31**, 1503 (2011).
- [17] J. C. Nappé, I. Monnet, Ph. Grosseau, F. Audubert, B. Guilhot, M. Beauvy, M. Benabdesselam, and L. Thomé, *J. Nucl. Mater.* **409**, 53 (2011).
- [18] J. C. Nappé, Ph. Grosseau, F. Audubert, B. Guilhot, M. Beauvy, M. Benabdesselam, and I. Monnet, *J. Nucl. Mater.* **385**, 304 (2009).
- [19] X. M. Liu, M. Le Flem, J.-L. Béchade, F. Onimus, T. Cozzika, and I. Monnet, *Nucl. Instrum. Meth. Phys. Res. B* **268**, 506 (2010).
- [20] K. R. Whittle, M. G. Blackford, R. D. Aughterson, S. Moricca, G. R. Lumpkin, D. P. Riley, and N. J. Zaluzec, *Acta Mater.* **58**, 4362 (2010).
- [21] E. H. Kisi, J. A. A. Crossley, S. Myhra, and M. W. Barsoum, *J. Phys. Chem. Solids* **59**, 1437 (1998).
- [22] M. W. Barsoum, T. El-Raghy, C. J. Rawn, W. D. Porter, H. Wang, E. A. Payzant, and C. R. Hubbard, *J. Phys. Chem. Solids* **60**, 429 (1999).
- [23] J. Emmerlich, H. Högberg, O. Wilhelmsson, U. Jansson, D. Music, J. M. Schneider, and L. Hultman, *Acta Mater.* **55**, 1479 (2007).
- [24] M. W. Barsoum, T. El-Raghy, and L. Ogbuji, *J. Electrochem. Soc.* **144**, 2508 (1997).
- [25] M. W. Barsoum, L. H. Ho-Duv, M. Radovic, and T. El-Raghy, *J. Electrochem. Soc.* **150**, B166-B175 (2003).
- [26] J. Travaglini, M. W. Barsoum, V. Jovic, and T. El-Raghy, *Corros. Sci.* **45**, 1313 (2003).
- [27] M. W. Barsoum and T. El-Raghy, *J. Am. Ceram. Soc.* **79**, 1953 (1996).
- [28] T. El-Raghy, M. W. Barsoum, A. Zavaliangos, and S. R. Kalidindi, *J. Am. Ceram. Soc.* **82**, 2855 (1999).
- [29] M. Radovic, M. W. Barsoum, T. El-Raghy, and S. M. Wiederhorn, *J. Alloys Compd.* **361**, 299 (2003).

- [30] T. Zhen, M. W. Barsoum, S. R. Kalidindi, M. Radovic, Z. M. Sun, and T. El-Raghy, *Acta. Mater.* **53**, 4963 (2005).
- [31] M. Le Flem, X. M. Liu, S. Doriot, T. Cozzika, and I. Monnet, *Int. J. Appl. Ceram. Technol.* **7**, 766 (2010).
- [32] J. F. Ziegler, J. P. Biersack, and U. Littmark, *The Stopping and Range of Ions in Solids*, Pergamon, New York (1985); available at <http://www.srim.org/>.
- [33] S. Thevuthasan, C. Peden, M. Engelhard, D. Baer, G. Herman, W. Jiang, Y. Liang, and W. Weber, *Nucl. Instrum. Meth. Phys. Res. A* **420**, 81 (1999).
- [34] R. Devanathan, W. J. Weber, and F. Gao, *J. Appl. Phys.* **90**, 2303 (2001).
- [35] W. K. Chu, J. W. Mayer, and M. A. Nicolet, *Backscattering Spectrometry*. Academic press, San Diego (1978).
- [36] W. Jiang, H. Wang, I. Kim, Y. Zhang, and W. J. Weber, *J. Mater. Res.* **25**, 2341 (2010).
- [37] Y. Zhang, W. Jiang, C. Wang, F. Namavar, P. D. Edmondson, Z. Zhu, F. Gao, J. Lie, and W. J. Weber, *Phys. Rev. B* **82**, 184105 (2010).
- [38] W. Jiang, J. A. Sundararajan, T. Varga, M. E. Bowden, Y. Qiang, J. S. McCloy, C. H. Henager, Jr., and R. O. Montgomery, *Adv. Funct. Mater.* **24**, 6210 (2014).
- [39] A. Audren, A. Benyagoub, L. Thomé, and F. Garrido, *Nucl. Instrum. Meth. Phys. Res. B* **257**, 227 (2007).
- [40] E. Friedland, N. G. van der Berg, T. T. Hlatshwayo, R. J. Kuhudzai, J. B. Malherbe, E. Wendler, and W. Wesch, *Nucl. Instrum. Meth. Phys. Res. B* **286**, 102 (2012).
- [41] J. C. Bourgoin and J. W. Corbett, *Rad. Eff.* **36**, 157 (1978).
- [42] J. R. Tesmer, M. Nastasi, J. C. Barbour, C. J. Maggiore, and J. W. Mayer, *Handbook of Modern Ion Beam Materials Analysis*, second edition, Materials Research Society, Pittsburgh, PA, 1995.
- [43] Y. Wang and M. Nastasi, *Handbook of Modern Ion Beam Materials Analysis*, second edition, Materials Research Society, Warrendale, PA, 2009.
- [44] A. Bellucci, D. Gozzi, M. Nardone, and A. Sodo, *Chem. Mater.* **15**, 1217 (2003).



**Pacific Northwest**  
NATIONAL LABORATORY

*Proudly Operated by **Battelle** Since 1965*

902 Battelle Boulevard  
P.O. Box 999  
Richland, WA 99352  
1-888-375-PNNL (7665)  
[www.pnnl.gov](http://www.pnnl.gov)



U.S. DEPARTMENT OF  
**ENERGY**